Research Article | Vol. 8, No. 10 | 1 Oct 2017 | BIOMEDICAL OPTICS EXPRESS 4348

Biomedical Optics EXPRESS

Noninvasive near infrared autofluorescence imaging of retinal pigment epithelial cells in the human retina using adaptive optics

TAO LIU,[1] HAEWON JUNG,[1] JIANFEI LIU,[1] MICHAEL DROETTBOOM,[2] AND JOHNNY TAM[1,*]

[1]*National Eye Institute, National Institutes of Health, Bethesda, MD 20892, USA*
[2]*Medical Science & Computing, Rockville, MD 20852, USA*
[*]*johnny@nih.gov*

Abstract: The retinal pigment epithelial (RPE) cells contain intrinsic fluorophores that can be visualized using infrared autofluorescence (IRAF). Although IRAF is routinely utilized in the clinic for visualizing retinal health and disease, currently, it is not possible to discern cellular details using IRAF due to limits in resolution. We demonstrate that the combination of adaptive optics (AO) with IRAF (AO-IRAF) enables higher-resolution imaging of the IRAF signal, revealing the RPE mosaic in the living human eye. Quantitative analysis of visualized RPE cells in 10 healthy subjects across various eccentricities demonstrates the possibility for *in vivo* density measurements of RPE cells, which range from 6505 to 5388 cells/mm^2 for the areas measured (peaking at the fovea). We also identified cone photoreceptors in relation to underlying RPE cells, and found that RPE cells support on average up to 18.74 cone photoreceptors in the fovea down to an average of 1.03 cone photoreceptors per RPE cell at an eccentricity of 6 mm. Clinical application of AO-IRAF to a patient with retinitis pigmentosa illustrates the potential for AO-IRAF imaging to become a valuable complementary approach to the current landscape of high resolution imaging modalities.

OCIS codes: (110.1080) Active or adaptive optics; (170.4470) Ophthalmology; (180.2520) Fluorescence microscopy; (110.3080) Infrared imaging; (170.3890) Medical optics instrumentation.

References and links

1. U. Kellner, S. Kellner, and S. Weinitz, "Fundus autofluorescence (488 nm) and near-infrared autofluorescence (787 nm) visualize different retinal pigment epithelium alterations in patients with age-related macular degeneration," Retina **30**(1), 6–15 (2010).
2. S. Schmitz-Valckenberg, D. Lara, S. Nizari, E. M. Normando, L. Guo, A. R. Wegener, A. Tufail, F. W. Fitzke, F. G. Holz, and M. F. Cordeiro, "Localisation and significance of in vivo near-infrared autofluorescent signal in retinal imaging," Br. J. Ophthalmol. **95**(8), 1134–1139 (2011).
3. C. N. Keilhauer and F. C. Delori, "Near-Infrared Autofluorescence Imaging of the Fundus: Visualization of Ocular Melanin," Invest. Ophthalmol. Vis. Sci. **47**(8), 3556–3564 (2006).
4. A. Ayata, S. Tatlipinar, T. Kar, M. Unal, D. Ersanli, and A. H. Bilge, "Near-infrared and short-wavelength autofluorescence imaging in central serous chorioretinopathy," Br. J. Ophthalmol. **93**(1), 79–82 (2009).
5. U. Kellner, S. Kellner, B. H. F. Weber, B. Fiebig, S. Weinitz, and K. Ruether, "Lipofuscin- and melanin-related fundus autofluorescence visualize different retinal pigment epithelial alterations in patients with retinitis pigmentosa," Eye (Lond.) **23**(6), 1349–1359 (2009).
6. S. Kellner, U. Kellner, B. H. F. Weber, B. Fiebig, S. Weinitz, and K. Ruether, "Lipofuscin- and Melanin-related Fundus Autofluorescence in Patients with ABCA4-associated Retinal Dystrophies," Am. J. Ophthalmol. **147**(5), 895–902 (2009).
7. M. B. Parodi, P. Iacono, C. Del Turco, and F. Bandello, "Near-Infrared Fundus Autofluorescence in Subclinical Best Vitelliform Macular Dystrophy," Am. J. Ophthalmol. **158**(6), 1247–1252 (2014).
8. J. Liang, D. R. Williams, and D. T. Miller, "Supernormal vision and high-resolution retinal imaging through adaptive optics," J. Opt. Soc. Am. A **14**(11), 2884–2892 (1997).
9. A. Roorda and J. L. Duncan, "Adaptive Optics Ophthalmoscopy," Annu Rev Vis Sci **1**(1), 19–50 (2015).
10. R. J. Zawadzki and D. T. Miller, "Retinal AO OCT," in *Optical Coherence Tomography*, W. Drexler and J. G. Fujimoto, eds. (Springer International Publishing, 2015), pp. 1849–1920.
11. A. Roorda, Y. Zhang, and J. L. Duncan, "High-Resolution In Vivo Imaging of the RPE Mosaic in Eyes with Retinal Disease," Invest. Ophthalmol. Vis. Sci. **48**(5), 2297–2303 (2007).

#298365 https://doi.org/10.1364/BOE.8.004348
Journal © 2017 Received 3 Jul 2017; revised 25 Aug 2017; accepted 29 Aug 2017; published 7 Sep 2017

Biomedical Optics EXPRESS

12. D. Scoles, Y. N. Sulai, and A. Dubra, "In vivo dark-field imaging of the retinal pigment epithelium cell mosaic," Biomed. Opt. Express **4**(9), 1710–1723 (2013).
13. Z. Liu, O. P. Kocaoglu, and D. T. Miller, "3D Imaging of Retinal Pigment Epithelial Cells in the Living Human Retina," Invest. Ophthalmol. Vis. Sci. **57**(9), OCT533 (2016).
14. J. I. W. Morgan, A. Dubra, R. Wolfe, W. H. Merigan, and D. R. Williams, "In Vivo Autofluorescence Imaging of the Human and Macaque Retinal Pigment Epithelial Cell Mosaic," Invest. Ophthalmol. Vis. Sci. **50**(3), 1350–1359 (2009).
15. J. Tam, J. Liu, A. Dubra, and R. Fariss, "In Vivo Imaging of the Human Retinal Pigment Epithelial Mosaic Using Adaptive Optics Enhanced Indocyanine Green Ophthalmoscopy," Invest. Ophthalmol. Vis. Sci. **57**(10), 4376–4384 (2016).
16. J. Tam, M. Droettboom, J. Liu, and H. Jung, "Noninvasive infrared autofluorescence imaging of intrinsic fluorophores in the human retina at cellular-level resolution using adaptive optics," Opt. Soc. Am. Bio-Opt. Des. Appl. JTu5A.1 (2017).
17. C. E. Granger, D. R. Williams, and E. A. Rossi, "Near-infrared autofluorescence imaging reveals the retinal pigment epithelial mosaic in the living human eye," Invest. Ophthalmol. Vis. Sci. **58**, 3429 (2017).
18. A. Dubra and Y. Sulai, "Reflective afocal broadband adaptive optics scanning ophthalmoscope," Biomed. Opt. Express **2**(6), 1757–1768 (2011).
19. *ANSI Z136.1 - 2014* (American National Standard for Safe Use of Lasers, Laser Institute of America, 2014).
20. E. A. Rossi, P. Rangel-Fonseca, K. Parkins, W. Fischer, L. R. Latchney, M. A. Folwell, D. R. Williams, A. Dubra, and M. M. Chung, "In vivo imaging of retinal pigment epithelium cells in age related macular degeneration," Biomed. Opt. Express **4**(11), 2527–2539 (2013).
21. A. G. Bennett and R. B. Rabbetts, "Proposals for new reduced and schematic eyes," Ophthalmic Physiol. Opt. **9**(2), 228–230 (1989).
22. D. Scoles, Y. N. Sulai, C. S. Langlo, G. A. Fishman, C. A. Curcio, J. Carroll, and A. Dubra, "In Vivo Imaging of Human Cone Photoreceptor Inner Segments," Invest. Ophthalmol. Vis. Sci. **55**(7), 4244–4251 (2014).
23. A. Dubra and Z. Harvey, "Registration of 2D Images from Fast Scanning Ophthalmic Instruments," in *Biomedical Image Registration*, B. Fischer, B. M. Dawant, and C. Lorenz, eds., Lecture Notes in Computer Science No. 6204 (Springer Berlin Heidelberg, 2010), pp. 60–71.
24. R. F. Cooper, M. A. Wilk, S. Tarima, and J. Carroll, "Evaluating Descriptive Metrics of the Human Cone Mosaic," Invest. Ophthalmol. Vis. Sci. **57**(7), 2992–3001 (2016).
25. J. L. Duncan, Y. Zhang, J. Gandhi, C. Nakanishi, M. Othman, K. E. H. Branham, A. Swaroop, and A. Roorda, "High-Resolution Imaging with Adaptive Optics in Patients with Inherited Retinal Degeneration," Invest. Ophthalmol. Vis. Sci. **48**(7), 3283–3291 (2007).
26. R. W. Rodieck, "The density recovery profile: A method for the analysis of points in the plane applicable to retinal studies," Vis. Neurosci. **6**(2), 95–111 (1991).
27. K. Y. Li and A. Roorda, "Automated identification of cone photoreceptors in adaptive optics retinal images," J. Opt. Soc. Am. A **24**(5), 1358–1363 (2007).
28. J. Liu, H. Jung, A. Dubra, and J. Tam, "Automated Photoreceptor Cell Identification on Nonconfocal Adaptive Optics Images Using Multiscale Circular Voting," Invest. Ophthalmol. Vis. Sci. **58**(11), 4477–4489 (2017).
29. J. Liu, A. Dubra, and J. Tam, "Computer-aided detection of human cone photoreceptor inner segments using multi-scale circular voting," in G. D. Tourassi and S. G. Armato, eds. Proc. SPIE **9785**, Medical Imaging 2016: Computer-Aided Diagnosis (2016), p. 97851A.
30. J. Liu, A. Dubra, and J. Tam, "A fully automatic framework for cell segmentation on non-confocal adaptive optics images," in G. D. Tourassi and S. G. Armato, eds. Proc. SPIE **9785**, Medical Imaging 2016: Computer-Aided Diagnosis (2016), p. 97852J.
31. C. A. Curcio, K. R. Sloan, R. E. Kalina, and A. E. Hendrickson, "Human photoreceptor topography," J. Comp. Neurol. **292**(4), 497–523 (1990).
32. M. A. Wilk, A. M. Dubis, R. F. Cooper, P. Summerfelt, A. Dubra, and J. Carroll, "Assessing the spatial relationship between fixation and foveal specializations," Vision Res. **132**, 53–61 (2017).
33. S. Panda-Jonas, J. B. Jonas, and M. Jakobczyk-Zmija, "Retinal Pigment Epithelial Cell Count, Distribution, and Correlations in Normal Human Eyes," Am. J. Ophthalmol. **121**(2), 181–189 (1996).
34. R. C. Watzke, J. D. Soldevilla, and D. R. Trune, "Morphometric analysis of human retinal pigment epithelium: correlation with age and location," Curr. Eye Res. **12**(2), 133–142 (1993).
35. T. Ach, C. Huisingh, G. McGwin, Jr., J. D. Messinger, T. Zhang, M. J. Bentley, D. B. Gutierrez, Z. Ablonczy, R. T. Smith, K. R. Sloan, and C. A. Curcio, "Quantitative Autofluorescence and Cell Density Maps of the Human Retinal Pigment Epithelium," Invest. Ophthalmol. Vis. Sci. **55**(8), 4832–4841 (2014).
36. H. Gao and J. G. Hollyfield, "Aging of the human retina. Differential loss of neurons and retinal pigment epithelial cells," Invest. Ophthalmol. Vis. Sci. **33**(1), 1–17 (1992).
37. A. M. Harman, P. A. Fleming, R. V. Hoskins, and S. R. Moore, "Development and aging of cell topography in the human retinal pigment epithelium," Invest. Ophthalmol. Vis. Sci. **38**(10), 2016–2026 (1997).
38. L. V. Del Priore, Y.-H. Kuo, and T. H. Tezel, "Age-related changes in human RPE cell density and apoptosis proportion in situ," Invest. Ophthalmol. Vis. Sci. **43**(10), 3312–3318 (2002).
39. B. W. Streeten, "Development of the human retinal pigment epithelium and the posterior segment," Arch. Ophthalmol. **81**(3), 383–394 (1969).

Biomedical Optics EXPRESS

40. L. Feeney-Burns, R. P. Burns, and C.-L. Gao, "Age-related macular changes in humans over 90 years old," Am. J. Ophthalmol. **109**(3), 265–278 (1990).
41. C. K. Dorey, G. Wu, D. Ebenstein, A. Garsd, and J. J. Weiter, "Cell loss in the aging retina. Relationship to lipofuscin accumulation and macular degeneration," Invest. Ophthalmol. Vis. Sci. **30**(8), 1691–1699 (1989).
42. M. O. Ts'o and E. Friedman, "The retinal pigment epithelium. III. growth and development," Arch. Ophthalmol. **80**(2), 214–216 (1968).
43. D. C. Gray, W. Merigan, J. I. Wolfing, B. P. Gee, J. Porter, A. Dubra, T. H. Twietmeyer, K. Ahamd, R. Tumbar, F. Reinholz, and D. R. Williams, "In vivo fluorescence imaging of primate retinal ganglion cells and retinal pigment epithelial cells," Opt. Express **14**(16), 7144–7158 (2006).
44. D. M. Snodderly, M. M. Sandstrom, I. Y.-F. Leung, C. L. Zucker, and M. Neuringer, "Retinal pigment epithelial cell distribution in central retina of rhesus monkeys," Invest. Ophthalmol. Vis. Sci. **43**(9), 2815–2818 (2002).
45. A. V. Cideciyan, M. Swider, and S. G. Jacobson, "Autofluorescence Imaging With Near-Infrared Excitation:Normalization by Reflectance to Reduce Signal From Choroidal Fluorophores," Invest. Ophthalmol. Vis. Sci. **56**(5), 3393–3406 (2015).
46. M. Boulton, "Ageing of the retinal pigment epithelium," Prog. Retinal Res. **11**, 125–151 (1991).

1. Introduction

Infrared autofluorescence (IRAF) is an increasingly-utilized clinical modality for visualization and monitoring of the health of the retinal pigment epithelial (RPE) cells in a variety of different diseases that include age-related macular degeneration [1–3], central serous chorioretinopathy [4], retinitis pigmentosa [5], ABCA4-associated retinopathies [6], Best vitelliform macular dystrophy [7], and others. Its clinical value is derived from the fact that it provides a complementary picture of retinal lesions, which from a macroscopic perspective appears to be similar to those visualized using other modalities (most typically compared to short-wavelength autofluorescence) but at a finer scale is often slightly or entirely distinct from other modalities [1,3,5–7]. Unraveling these microscopic nuances could reveal new insights about the mechanisms of disease. However, the resolution that is provided by commercially-available conventional IRAF instruments is currently not sufficient to visualize cellular detail.

Adaptive optics (AO) is a technology developed over the past two decades that has been used to achieve higher resolution by correcting for ocular aberrations [8]. When combined with imaging platforms, AO ophthalmoscopes have the capabilities to resolve fine cellular details of the living human retina [9,10]. There are now a number of approaches that utilize AO for imaging RPE cells, based on capturing intrinsic scattering of light [11,12], generating contrast derived from organelle motility [13], visualizing autofluorescence of lipofuscin [14], and imaging fluorescent labeling by intravenously-injected indocyanine green dye [15]. Recently, we and others have independently reported that the integration of AO with IRAF can also be used to resolve individual RPE cells [16,17].

In this paper, we improve upon our previous report [16] by demonstrating that our current implementation of AO-IRAF can be used to visualize RPE cells at eccentricities ranging from the fovea out to at least 6 mm, utilizing exposure times that are on the order of 9-12 seconds per video. We also quantified RPE cell density and spacing from the living human eye in a cohort of healthy subjects, which will be important for future comparisons to measurements from diseased eyes. Our preliminary clinical investigations illustrate how AO-IRAF might be useful for intuitively linking observed cellular-level changes with the macroscopic clinical picture.

2. Methods

2.1 Instrumentation

A custom-built adaptive optics scanning light ophthalmoscope [18] that had been previously-modified to detect fluorescence light from indocyanine green (ICG) (described in more detail in [15]) was further modified to improve detection of IRAF light, which shares similar excitation and emission bands. The excitation and emission spectra of our instrument were designed to closely match those of a commercially-available instrument with IRAF imaging

Biomedical Optics EXPRESS

capabilities (see next paragraph). We used 20-30 µW of 850 nm light (central wavelength 845 nm, 23.7 nm full width at half maximum, product SLD-MS-381-MP-SM-850; Superlum, Ireland) for wavefront sensing and 115-130 µW of 790 nm light (central wavelength 794.3 nm, 16.1 nm full width at half maximum, product S-790-G-I-15-M; Superlum, Ireland) for excitation (7.75 mm beam diameter; all powers measured at the cornea) which combined are below the maximum permissible exposure set by the American National Standards Institute standard Z136.1-2014 [19]. Power levels were fixed for each imaging session, but varied from session to session due to instrument alignment. Since the AO-IRAF signal is at least several-fold weaker than the AO-ICG signal [15], detection of fluorescent light in the 810-830 nm band was further enhanced by redesigning our computer-controlled fixation system [20] to utilize a large dichroic (cut-off wavelength 596 nm, product FF596-Di01, Semrock, Rochester, NY), which transmits a higher percentage of light in the 810-830 nm band than the 90/10 pellicle beamsplitter that we previously utilized for our AO fixation system. We also increased the size of the confocal pinhole that was used for detection of IRAF light from 3 Airy Units to either 6 or 8 Airy Units.

A commercially-available scanning laser ophthalmoscope (Heidelberg Spectralis HRA + OCT, Heidelberg, Germany) was used to capture conventional IRAF images for comparison to AO-IRAF. This instrument utilizes a 788 nm light source with average power 2.5 mW measured at the cornea for excitation, and detects autofluorescence in the band 805-840 nm.

Biometry measurements (axial length, corneal curvature, and anterior chamber depth) were also measured in all subjects using an IOL Master (Carl Zeiss Meditec, Dublin, CA, USA) and used to compute a retinal scaling factor from degrees to millimeters based on a paraxial ray trace on a three-surfaced simplified eye model [21].

2.2 Human subjects

Research procedures adhered to the tenets of the Declaration of Helsinki and were approved by the local Institutional Review Board (National Institutes of Health). Written informed consent was obtained after the nature of the research and possible consequences of the study were explained.

We recruited human subjects to undergo adaptive optics imaging through the National Institutes of Health (NIH) Clinical Center. Healthy subjects had 20/20 or better vision and no history or signs of ocular disease. For the healthy subjects, we retrospectively selected a subset of subjects for this paper which were previously imaged primarily for the purpose of acquiring normative cone photoreceptor data (i.e. short acquisition times, 9-12 seconds corresponding to 150-200 frames, were used at most locations), and then reanalyzed the data to evaluate the AO-IRAF signal. We first restricted the analysis to only those subjects that were imaged using the modified AO-IRAF instrument described above (n = 29 subjects). From this cohort, eligible subjects for inclusion into this study were those that had images taken along the temporal meridian (n = 16) and in addition those that had refractive errors less than ± 5.00 D spherical equivalent (n = 13). Additional details about these subjects are provided in Table 1. Since the conventional IRAF signal is largely homogeneous at the length scales that we image over, we also examined imaging data from patients with retinal diseases. Here, our goal was to evaluate areas of hyper- and hypo-fluorescence using AO-IRAF in the context of conventional IRAF imaging. We selected one patient diagnosed with retinitis pigmentosa that we had previously imaged and reanalyzed their data set for AO-IRAF content. Conventional IRAF images were acquired in all but one subject due to the instrument not being available on the day of the visit (noted in Table 1).

2.3 Image acquisition and processing

Prior to imaging, eyes were dilated with 2.5% phenylephrine hydrochloride and 1% tropicamide. Videos were acquired using multiple square fields of view (ranging from

Biomedical Optics EXPRESS

Table 1. Overview of Healthy Subjects

ID	Age	Eye	Sex	Refractive Error [D]	AL [mm]	Spectralis IRAF	AO-IRAF signal	RPE cell analysis
1	32	OS	M	Plano	23.53	Yes	Yes	Yes
2	23	OD	F	Plano	23.77	Yes	Yes	Yes
3	25	OS	F	–1.00, + 0.00	24.74	Yes	Yes	Yes
4	23	OD	F	+ 1.75, + 0.00	22.45	N/A	Yes	Yes
5	21	OS	F	Plano	24.01	Yes	Yes	No
6	22	OD	F	–1.00, + 0.50x164	23.82	No	No	No
7	26	OS	F	–1.00, + 0.25x75	23.37	Yes	Yes	Yes
8	22	OD	M	Plano	23.27	Yes	Yes	Yes
9	35	OS	M	+ 0.75, + 0.75x100	22.05	Yes	Yes	Yes
10	40	OD	M	–2.00, + 1.75x93	23.64	Yes	Yes	Yes
11	23	OD	F	Plano	24.01	Yes	Yes	Yes
12	24	OS	F	Plano	22.85	Yes	Yes	Yes
13	40	OS	F	+ 0.75, + 0.25x51	22.67	Yes	Yes	No

Expanded descriptions: ID: subject identification number; AL: axial length; Spectralis IRAF: indicates whether a conventional IRAF signal could be captured (N/A indicates test was not performed); AO-IRAF signal: indicates whether a macroscopic AO-IRAF signal was visible after re-analysis of data; RPE cell analysis: indicates whether the quality of the AO-IRAF signal was high enough to perform the RPE cell identification analysis.

approximately 0.23 to 0.45 mm on the retina) at various overlapping retinal locations from the fovea out to an eccentricity of approximately 6 mm in the temporal direction (approximately 100-150 videos per subject). For each subject, we acquired short videos (9-12 seconds) at each retinal location. Additionally, we collected long videos (30-120 seconds) at the fovea, 5°, 10°, and 15° temporal retina whenever possible. At each retinal location, four imaging channels were simultaneously acquired (confocal reflectance [18], split detection [22], darkfield [12], and AO-IRAF).

Videos were stabilized to correct for eye motion using the confocal channel [14,23] and then averaged and assembled into montages that included the multiple simultaneously-acquired channels. We also developed a global averaging approach for the AO-IRAF channel in which overlapping regions of locally-averaged images were in turn averaged together in order to enhance AO-IRAF signal at areas of overlap. Finally, AO-IRAF image histograms were stretched for display purposes.

2.4 Image analysis

Using the confocal reflectance channel in each montage, the fovea was subjectively marked based on the estimated location of highest cone density. Next, 100 µm x 100 µm regions of interest (ROIs) from the AO-IRAF channel were selected from the montage up to 6 mm with a 0.5 mm interval. RPE cells were manually identified within these ROIs. To calculate RPE cell density, Voronoi diagrams were constructed for each ROI using the manually-identified points and then the number of identifications was divided by the total area of the corresponding Voronoi neighborhoods (excluding those neighborhoods which exceeded the boundary of the ROI). The RPE cell-to-cell spacing was estimated according to a previously-developed implementation [24] of the density recovery profile [25,26].

In addition, simultaneously-acquired confocal and split detection images were analyzed to identify cone photoreceptors in relation to RPE cells visualized using AO-IRAF, across various eccentricities. Cone photoreceptors were identified semi-automatically, based on previously-published algorithms combined with manual correction [27–30]. In the fovea, a smaller sampling window (37µm × 37µm) within the initial ROI was selected to mitigate the effects of the large variation in cone density in the fovea [31,32]. This smaller ROI was then

Biomedical Optics EXPRESS

slightly enlarged to include the full extent of underlying Voronoi segments that were mostly residing (>50%) within the initial cone ROI.

3. Results

3.1 AO-IRAF images reveal macroscopic lesions with cellular-level resolution

Macroscopic features observed using AO-IRAF corresponded well to those observed using conventional IRAF in a patient with retinitis pigmentosa (Fig. 1). There was a clear improvement in the resolution of the AO-IRAF images when compared to the conventional IRAF images, and the fine details of most hypofluorescent areas could be better delineated using AO-IRAF (Fig. 1(D), 1(F)). Although the RPE mosaic was not visible in the fovea of this patient (Fig. 1(H)), it was visible in other portions of the AO-IRAF montage (for example in Fig. 1(D), 1(F)). In some areas, small hypofluorescent areas could be seen on the AO-IRAF image but not on the conventional IRAF image (arrows, Fig. 1). The local similarity between AO-IRAF and IRAF in this paper is consistent with data shown in our previous report [16] and confirms that we are measuring the same signal with these two techniques.

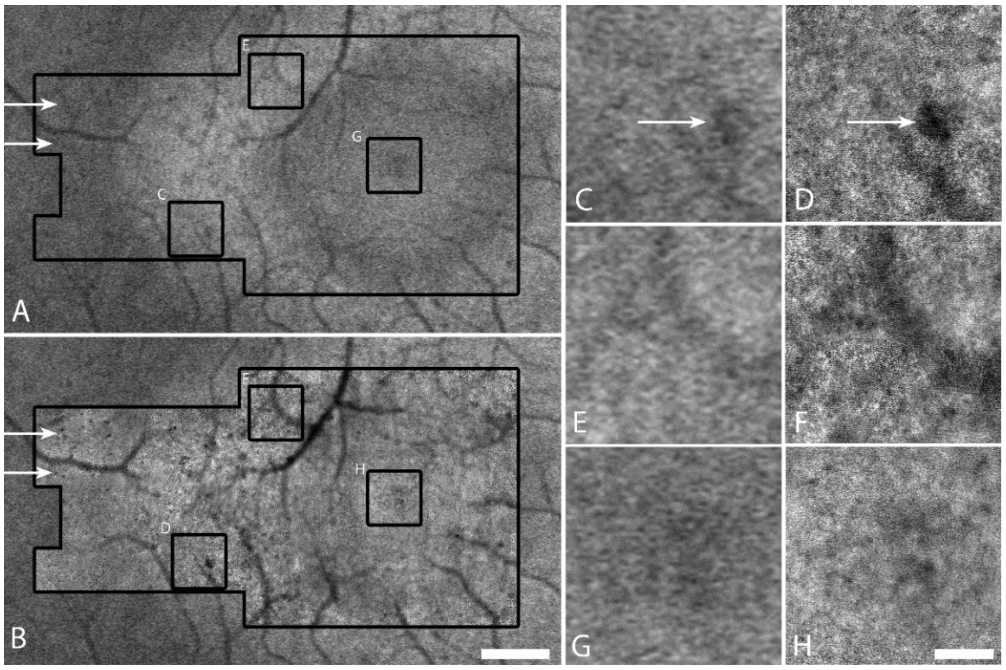

Fig. 1. Comparison of conventional IRAF to AO-IRAF for a patient with retinitis pigmentosa. (A) Conventional IRAF image acquired using a Heidelberg Spectralis. Black outline shows the location where AO-IRAF images were taken. (B) AO-IRAF montage (inside larger black outline) overlaid on the conventional IRAF image. Scale bar, 0.5 mm. (C-H) Zooms of three areas outlined by the small black squares in (B) comparing conventional IRAF (C,E,G) to AO-IRAF (D,F,H). Scale bar, 100 µm. The RPE mosaic is visible in (D) and (F) in some portions of the image. Additional details about hypofluorescent areas can be observed using AO-IRAF (arrows). The hyperfluorescent ring in (A) is less visible in (B) due to the stretching of each individual image within the AO-IRAF montage, an artifact of montaging.

3.2 AO-IRAF reveals individual RPE cells

The RPE mosaic could be visualized at the fovea using long exposure videos (30-120 seconds), consistent with our previous report showing foveal RPE cells in three additional healthy subjects [16]. In order to verify that these cells were in fact RPE cells, in one subject (subject 10) we carried out a direct comparison between AO-IRAF and darkfield imaging (Fig. 2). There was very good correspondence between the outlines of RPE cells seen in both

Biomedical Optics EXPRESS

modalities (Fig. 2(C)). Interestingly, there were some lower frequency components of the images (i.e. a few cell widths in size) that also seemed to colocalize across the two channels.

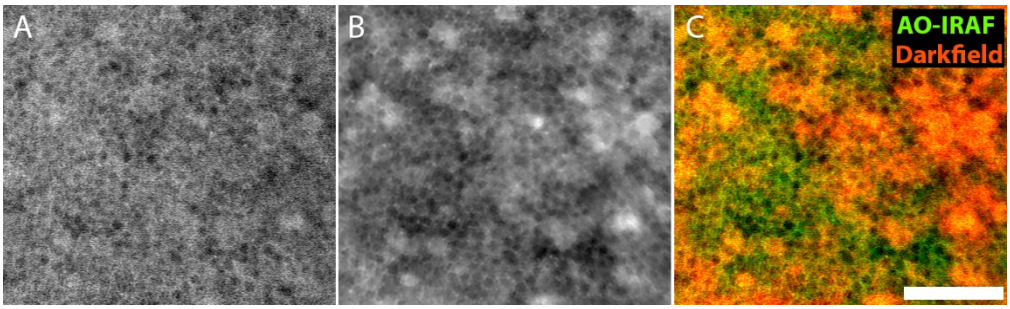

Fig. 2. Comparison of foveal RPE cells imaged using (A) AO-IRAF and (B) darkfield in subject 10. Images were simultaneously acquired and are exactly registered with each other. (C) False color image showing the AO-IRAF image in green and darkfield image in red. Outlines of RPE cells are colocalized with each other. Scale bar, 50 µm.

3.3 AO-IRAF can be used to map the RPE density/spacing across different eccentricities

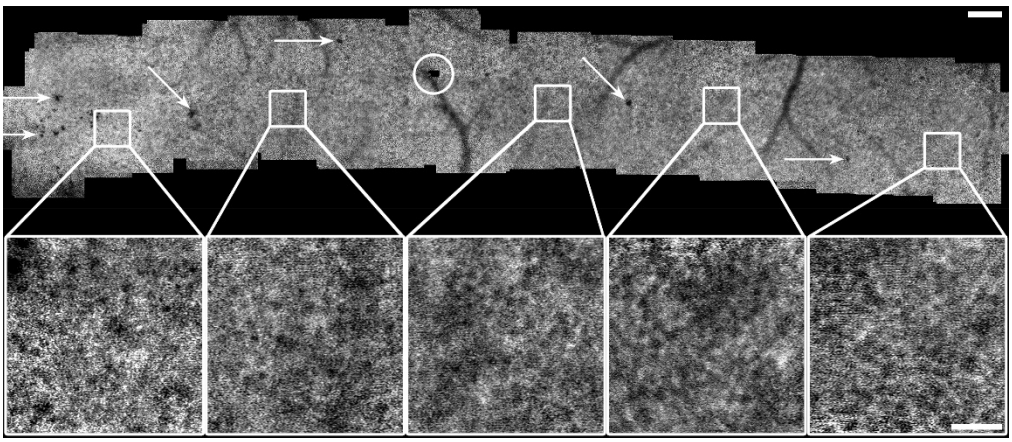

Fig. 3. The RPE mosaic can be visualized across the temporal meridian using AO-IRAF acquired using short exposures (this montage was constructed from 145 overlapping videos, each with an acquisition time of 9 seconds; subject 7). There are some small patches of hypofluorescence throughout the retina which were also visualized in many of the other healthy subjects (arrows). One small area which was not covered during AO imaging (circle). Scale bars: 200 µm (top), 50 µm (bottom).

Macroscopic signals were visualized in the AO-IRAF data for all but one of the healthy subjects (Table 1). Even though short acquisition times were used for most video locations, RPE cells could still be visualized and analyzed across multiple eccentricities for 10 out of 13 healthy subjects (Figs. 3, 4; Tables 2, 3). For the short acquisition times, visualization of the RPE mosaic was most successful at eccentric locations (approximately 2.5 to 3.5 mm; Fig. 4(C)). In contrast, for most subjects, the foveal RPE mosaic required long acquisition times. We manually identified RPE cells wherever possible and computed density and spacing statistics across different eccentricities. In general, the RPE density decreased with eccentricity (Fig. 4(A)), while the cell-to-cell spacing increased (Fig. 4(B)). In this cohort (n = 10; age 27.4 ± 6.9, mean ± SD) we found a range of RPE cell densities peaking at an average of 6505 cells/mm^2 in the fovea to 5388 cells/mm^2 at an eccentricity of 5 mm. The RPE cell-to-cell spacing varied from 14.02 µm in the fovea to 16.39 µm at an eccentricity of 5 mm.

Biomedical Optics EXPRESS

Overall, there was large variability (large standard deviations) reported across all studies, ostensibly due to large intersubject variability. Taking this into consideration, our AO-IRAF-based measurements are comparable to existing *ex vivo* measurements of RPE cell density and spacing from histological studies [33–42] as well as to *in vivo* measurements using other imaging modalities [13–15,22]. At the fovea, our density results are lower than Gao and Ach's measurements, while higher than the results of Watzke and Panda-Jonas (Fig. 4(A)). Between 1.5 and 4.5mm, our density results are in agreement with Morgan's measurements (from short-wavelength AO autofluorescence), but higher than other studies. Above 5 mm, our density measurements are higher than previously-published values. In terms of spacing, our data is consistent with the measurements of Ts'o [42] and Watzke [33] at fovea and those of Ach [35] and Liu [13] in the periphery. There were two other *in vivo* studies [12,14] that reported smaller spacing values. Nevertheless, our spacing measurements are within the range of variability of previous studies.

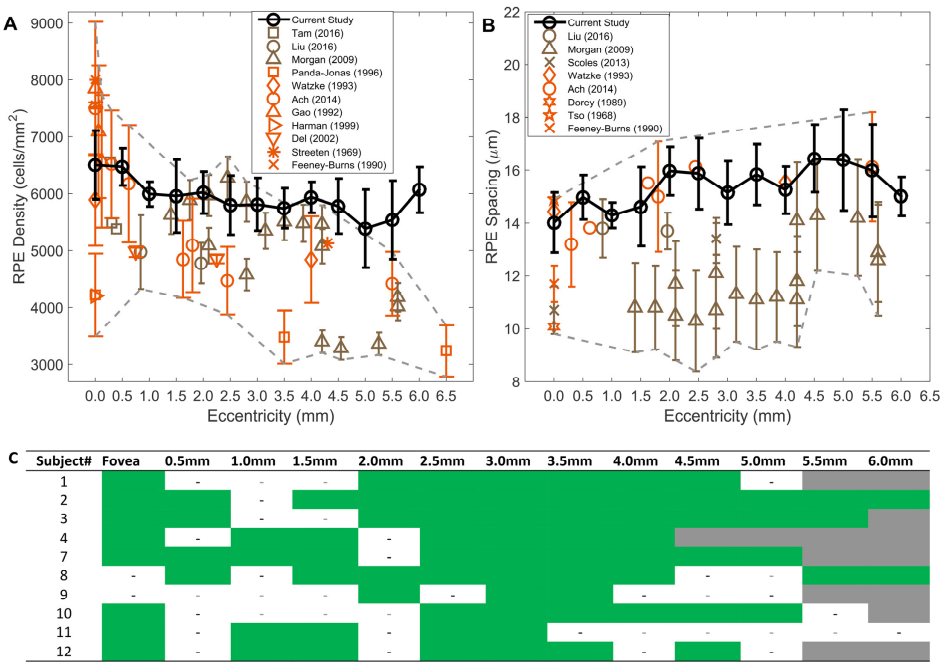

Fig. 4. Comparison of AO-IRAF-based measurements of RPE cell density and cell-to-cell spacing (black) with previously-published data from *in vivo* (umber color) and *ex vivo* (persimmon color) studies. Symbols denote the mean value averaged over all subjects from each study, and error bars show standard deviation. For comparison, published data with a mean age less than 50 years were selected wherever possible, with the exceptions of Feeney-Burns (mean age 58.9 ± 7.4 years) and Panda-Jonas (58.6 ± 18 years). The region showing the range (within 1 SD) of all published data combined is delineated by the gray dashed lines. (A) RPE density measurements. (B) RPE cell-to-cell spacing measurements. Note that only direct measurements of spacing are included, and in particular no spacing values are inferred from density based on the assumption of a perfectly triangularly-packed mosaic, due to the previously-reported decrease in regularity at the peripheral locations [14]. (C) The subset of regions with a contiguous array of RPE cells that could be identified for this analysis is shown in green; areas that were imaged but not analyzable are labeled with small dashed lines. Retinal locations that were not imaged are shown in gray.

3.4 Multimodal AO imaging enables photoreceptor-RPE comparative studies

The primary imaging objective for this cohort of healthy subjects was to acquire normative photoreceptor data, and as such the focal plane was set to optimize photoreceptor image

Biomedical Optics EXPRESS

quality. Since the AO-IRAF channel was acquired alongside these other channels simultaneously, this enables precise comparisons to be made between individual RPE cells and their overlying photoreceptors (all channels are in near-exact registration since a single imaging light source is used for all channels). To demonstrate this capability, we manually identified RPE cells and photoreceptor cells across multiple eccentricities on the same cohort of healthy subjects (N = 10) and quantified the average number of cone photoreceptor cells that were served by individual RPE cells (Fig. 5). Some regions could not be analyzed due to poor image quality on either the confocal or split detection channels.

The cone photoreceptor cell to RPE cell ratio was roughly 19:1 near fovea, rapidly declining to about 2:1 by 2 mm temporal to fovea (Fig. 6). The ratio in the parafovea varies less, and by 6 mm from fovea, stabilizes around 1:1. Overall, our measured ratios are in agreement with previous studies in both humans and primates [13,14,33,36,40,41,43,44]. The foveal ratio had the largest intersubject variability, partially due to the location of our sampling windows which varied from 0.08 to 0.15 mm from the foveal center [31]. Aside from some variability at the fovea (Gao et al [36] reported a ratio of 22.7:1 at the fovea, similar to our measurements, whereas Dorey [41] and Feeney-Burns [40] reported ratios of 12.7:1 and 5.8:1, respectively, a factor of 1.5 and 3.2 lower than our measurement) and also some differences between our results and measurements from two animal studies which might or might not faithfully recapitulate the situation in humans [14,43], all other studies reported ratios very close to our results.

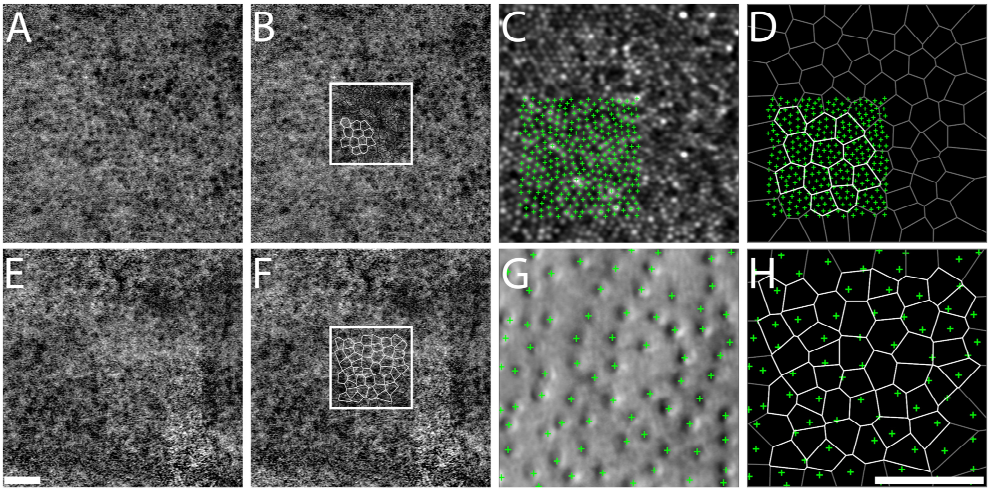

Fig. 5. Relationship between RPE cells visualized using AO-IRAF (A,B,E,F) and overlying cone photoreceptors visualized using confocal reflectance (C) in the fovea and split detection at eccentric locations (G), illustrated in subject 3. Panels (B) and (F) depict ROIs selected for analysis from (A) and (E), with Voronoi boundaries calculated from the estimated cell centers overlaid (white lines indicate the actual Voronoi regions that were used for analysis; black lines, not used). The size of the ROI was further reduced in the fovea (C). Cone identifications were plotted relative to RPE cell voronoi neighborhoods (D,H) to quantify the average number of cone photoreceptors per RPE cell. Scale bar, 50 µm.

Biomedical Optics EXPRESS

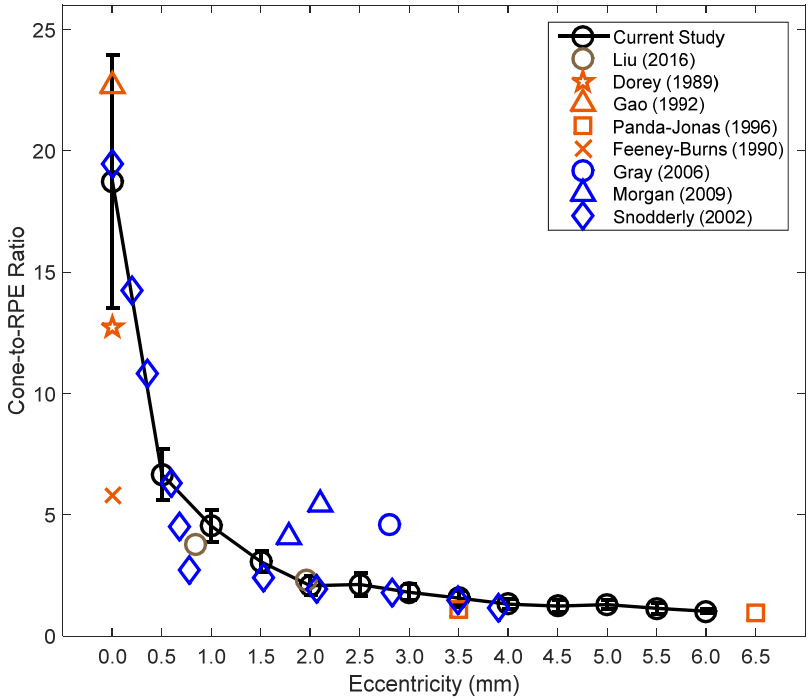

Fig. 6. Relationship between RPE cells and photoreceptor cells along temporal eccentricity from the fovea with previously published data from *in vivo* (umber color) and *ex vivo* (persimmon color) human studies as well as from animal studies (blue color). Symbols denote the mean value averaged over all subjects from each study. Error bars represent the standard deviation.

4. Discussion

AO-IRAF provides a natural link between the cellular world revealed by AO and the tissue-level length scale imaged by existing clinical modalities. These two worlds are often difficult to relate to each other, as in the case of AO scanning light ophthalmoscopy [18] vs. scanning laser ophthalmoscopy (e.g. Heidelberg Spectralis), where striking differences in the level of detail make it difficult to directly transfer clinical expertise into the ability to interpret AO images. However, the similarity between AO-IRAF and IRAF (Fig. 1 and other clinical examples shown in our previous report [16]) provides an intuitive way to interpret and analyze AO-IRAF images, but with enhanced details about areas of abnormal autofluorescence. All in all, pairing AO-IRAF with IRAF should lead to new insights about the pathophysiology of disease.

For most AO ophthalmoscopes that utilize near-infrared imaging light sources, AO-IRAF can be implemented without substantial modification to the instrument by adding an additional detection arm to capture autofluorescent signal that would otherwise have been discarded. In particular, no additional light sources are needed, which is an important light safety consideration. In fact, our results demonstrate that AO-IRAF can be collected without sacrificing the quality of photoreceptor imaging, using short acquisition times in the same plane of focus as that which would have been used for imaging photoreceptors. Thus, one can begin to explore the health of other cells in the retina using this multimodal AO approach (e.g. cone photoreceptor / RPE relationships as shown in Fig. 5).

Biomedical Optics EXPRESS

Although we could only find a small handful of examples (out of hundreds of images) in which darkfield images revealed the RPE mosaic, side-by-side comparison of AO-IRAF and darkfield images of RPE cells in one healthy subject showed good correspondence between the two (Fig. 2). RPE cells visualized using darkfield have also been previously shown to colocalize with two other modalities (AO short-wavelength autofluorescence [12] and AO-ICG [15]). This is consistent with a recent report that AO-IRAF directly colocalizes with AO short-wavelength autofluorescence [17]. Compared to darkfield images [12], AO-IRAF has a higher success rate across the retina; in our hands, it is difficult to use darkfield to visualize RPE cells at non-foveal locations [15]. The IRAF signal is thought to arise from melanin [3,45], while the short-wavelength autofluorescence is thought to originate from lipofuscin. Thus, the two modalities provide complementary information about the RPE in retinal pathologies. Although individual RPE cells could be visualized by short-wavelength [14] and near-infrared autofluorescence, the latter is potentially safer for patients who may be vulnerable to photochemical damage; it is also advantageous in terms of patient comfort (patient perceives a dim light as opposed to a bright one). Our measurements of RPE cell density and spacing using AO-IRAF were similar to the expected values from histology (Fig. 4). These results, together with our previously-reported results showing good correspondence between RPE cells visualized using AO-IRAF, confocal reflectance, and darkfield in a patient with retinitis pigmentosa who had a retinal region devoid of overlying photoreceptors [16], support our claim that we are visualizing RPE cells.

The majority of our quantitative measurements are comparable with previously-published data. However, there are some discrepancies, which could arise from a number of different factors. First, the intersubject variability of the RPE mosaic is particularly noticeable in both our data as well as data from previous studies; different study populations will introduce sampling artifacts. Some studies have suggested that RPE density decreases with age [33,40,41], which might explain why the density values in our cohort are higher than those of Panda-Jonas (mean age of 27.4 compared to Panda-Jonas' cohort with mean age 58.6). In addition, the method used to count RPE cells may also lead to bias. For example, some histological studies [40,41] considered each nucleus to be equivalent to a cell, which could lead to overestimations of density in the case of large numbers of multinucleated RPE cells [41], and underestimation of the cone-to-RPE ratio. The existence of this large variation in the literature points to the value of noninvasive, *in vivo* measurements to longitudinally assess and monitor differences over time in healthy subjects and to reveal the disease progression in patients with suspected RPE damage.

Our multimodal AO imaging approach allows *in vivo* comparative measurements between cones and RPE cells which may have important implications in evaluating diseases that affect one or the other or both. As far as we know, this is the first report of measurements of cone-RPE ratios across a large range of retinal eccentricities in the living human eye. This ratio might be useful for understanding whether changes in the phagocytic and metabolic loads on individual RPE cells occur in disease or aging (for example, an abnormally high ratio could indicate a larger than normal phagocytic load leading to faster accumulation of byproducts such as lipofuscin that could in turn accelerate photoreceptor death [36,41,46]). Although this study did not address the rod to RPE ratio, future work using our multimodal AO approach could enable better measurements of RPE load that may be more predictive of detecting vision loss at the cellular level. Nevertheless, the cone to RPE ratio might be useful as an indicator of the health of the photoreceptor-RPE complex at the fovea in the context of geographic atrophy and other macular diseases.

We acknowledge that an inherent limitation of this study is that RPE cells could not be visualized at some retinal eccentricities. This is partly due to the retrospective nature of this study. Regional differences in melanin content might also affect the ability of AO-IRAF to visualize RPE cells (our highest success rate was around eccentricities between 2.5 to 3.5 mm). That said, for all but the largest two eccentricities of this study, we had coverage of at

Biomedical Optics EXPRESS

least four different subjects (Tables 2, 3, 4). Future work includes further optimization of the image acquisition protocol and the AO-IRAF signal, which should help to improve the overall success rate of this technique for visualizing individual RPE cells. We expect that the use of slightly longer acquisition times, particularly in the foveal regions, will improve the ability of AO-IRAF to visualize cellular detail across the entire retina (in all subjects, there were areas in which we could not visualize cellular detail). Nevertheless, despite the use of shorter acquisition times, we were able to visualize a macroscopic AO-IRAF signal whenever a conventional IRAF signal could also be captured. We found that by increasing the pinhole size used for AO-IRAF from 3 to 6 Airy Units, that the signal was approximately 40% higher. The success rate of AO-IRAF was greatly improved by the ability to correct for eye motion from a different imaging channel (not possible in the Heidelberg Spectralis) and through the use of our global averaging approach, which helped us to enhance the signal in the overlapping video locations. However, in some instances, we opted to forgo global averaging to better visualize cellular detail (we found that the presence of small errors in image-to-image registration during the montaging step or larger-than-expected distortions inherent within each image could sometimes deteriorate images after global averaging). Finally, we collected only a narrow bandwidth of autofluorescent light (from 810 to 830 nm); we expect that by collecting autofluorescent light over a wider bandwidth that the AO-IRAF signal will be further enhanced. These future improvements should help to further improve upon the clinical applicability of AO-IRAF which we have started to demonstrate in this paper (Fig. 1).

5. Conclusion

We present a novel AO modality that can reveal cellular detail in the context of an established clinical modality, providing the ability to zoom in at a finer level of detail to better understand how microscopic changes contribute to clinical manifestations of disease.

Appendix

Table 2. RPE cell density in cells/mm^2 at different retinal eccentricities.

Subject	Eccentricity (mm)												
#	Fovea	0.5	1.0	1.5	2.0	2.5	3.0	3.5	4.0	4.5	5.0	5.5	6.0
1	5805	-	-	-	6325	6088	6077	5988	5783	5718	-		
2	6207	5990	-	5791	5443	5276	5724	5599	5702	6443	5889	6326	5788
3	7496	6648	-	-	5889	6073	6184	6175	6426	5800	4688	5253	
4	6088	-	5722	5490	-	4936	5334	4955	5676				
7	6479	6537	6142	6728	-	5377	6356	5900	6149	6160	6050		
8	-	6720	-	5100	6289	6305	5824	5974	5890	-	-	5043	6351
9	-	-	-	-	6165	-	6461	5740	-	-	-		
10	7017	-	-	-	-	5827	5121	5685	5942	5066	4923	-	
11	5946	-	6189	5990	-	5766	5273	-	-	-	-	-	-
12	6996	-	5924	6657	-	6543	5793	5688	-	5508	-		

The small dashed lines indicate retinal locations where a contiguous array of RPE cells could not be identified. Retinal locations that were not imaged are marked in gray.

Biomedical Optics EXPRESS

Table 3. RPE cell spacing in µm at different retinal eccentricities.

Subject	Eccentricity (mm)												
#	Fovea	0.5	1.0	1.5	2.0	2.5	3.0	3.5	4.0	4.5	5.0	5.5	6.0
1	15.8	-	-	-	16.7	15.4	14.7	15.1	15.8	17.3	-		
2	16.1	15.1	-	14.8	16.9	18.5	14.8	15.9	15.2	17.4	16.3	14.5	15.5
3	14.1	14.9	-	-	13.9	15.1	15.1	16.5	14.6	15.8	17.7	15.6	
4	13.0	-	13.8	14.2	-	16.5	16.5	17.7	15.3				
7	15.1	13.2	14.1	13.3	-	17.3	16.4	15.9	13.8	14.4	13.7		
8	-	13.4	-	17.5	13.4	14.8	15.2	13.4	14.2	-	-	17.9	14.5
9	-	-	-	-	13.2	-	13.7	16.0	-	-	-		
10	14.2	-	-	-	-	15.8	13.3	15.8	16.6	17.8	17.8	-	
11	12.6	-	15.0	14.3	-	14.2	14.7	-	-	-	-	-	-
12	12.9	-	14.3	13.6	-	15.2	17.0	15.3	-	15.9	-		

The small dashed lines indicate retinal locations where a contiguous array of RPE cells could not be identified. Retinal locations that were not imaged are marked in gray.

Table 4. Cone:RPE ratio at different retinal eccentricities.

Subject	Eccentricity (mm)												
#	Fovea	0.5	1.0	1.5	2.0	2.5	3.0	3.5	4.0	4.5	5.0	5.5	6.0
1	25.0	-	-	-	2.4	2.1	2.0	1.8	1.6	1.5	-		
2	-	7.8	-	2.9	2.1	1.8	1.5	1.4	1.1	0.9	1.1	1.1	1.1
3	14.9	-	-	-	2.2	1.7	1.5	1.4	1.1	1.0	1.3	1.0	
4	-	-	5.0	3.2	-	2.8	2.3	2.1	1.5				
7	12.1	5.7	4.2	3.1	-	3.0	2.0	1.9	1.5	1.5	1.4		
8	-	6.5	-	3.7	2.2	2.1	1.6	1.6	1.2	-	-	1.4	1.0
9	-	-	-	-	1.4	-	1.4	1.3	-	-	-		
10	22.1	-	-	-	-	2.1	2.2	1.6	1.4	1.5	1.5	-	
11	-	-	5.2	3.2	-	2.2	1.8	-	-	-	-	-	-
12	19.5	-	3.8	2.4	-	1.5	1.8	1.2	-	1.1	-		

The small dashed lines indicate retinal locations where either IRAF or confocal/split channel image quality was too poor for reliable cell identification. Retinal locations that were not imaged are marked in gray.

Funding

This research was supported by the Intramural Research Program of the NIH, National Eye Institute.

Acknowledgments

The authors would like to thank Laryssa Huryn, Catherine Cukras, Wadih Zein, Angel Garced, Gloria Babilonia-Ayukawa, John Rowan, Patrick Lopez, Sharon Yin, Christina Appleman, and Denise Cunningham for assistance with clinical procedures, Robert Cooper, Pavan Tiruveedhula, and Austin Roorda for sharing cone photoreceptor analysis software, and Alfredo Dubra for assistance with optimizing non-IRAF portions of the AO instrumentation. Portions of this work were presented at the OSA Optics in the Life Sciences Conference in 2017, JTu5A.1.

Disclosures

The authors declare that there are no conflicts of interest related to this article.